Chapter 3 Atmospheric and Marine Environment Monitoring

3.1 Monitoring of greenhouse gases[28]

- ○ Concentrations of carbon dioxide both in the air and in oceans are increasing.
- ○ Concentrations of atmospheric methane have shown an ongoing increase (with the exception of a stationary phase from 1999 to 2006).
- ○ Concentrations of atmospheric nitrous oxide are increasing.

JMA operates the World Data Centre for Greenhouse Gases (WDCGG)[29] to collect, maintain and provide data on greenhouse gases for related monitoring on a global scale under the Global Atmosphere Watch (GAW) Programme of the World Meteorological Organization (WMO). Analysis of data reported to WDCGG shows that the global mean concentration of greenhouse gases with strong impacts on global warming (in particular, carbon dioxide (CO_2), methane (CH_4) and nitrous oxide (N_2O)) continues to increase (Table 3.1-1).

In Japan, JMA monitors surface-air concentrations of greenhouse gases via three observation stations at Ryori in Ofunato, Minamitorishima in the Ogasawara Islands and Yonagunijima in the Nansei Islands. In the western North Pacific, JMA's research vessels observe oceanic and atmospheric CO_2. In addition, sampling of greenhouse gases in upper-air areas using cargo aircraft was commenced in 2011 (Figure 3.1-1).

Table 3.1-1 Atmospheric concentrations of major greenhouse gases (2017)[30]

	Atmospheric mole fraction			Absolute increase from 2016	Relative increase from 2016	Lifetime
	Pre-industrial level around 1750	Global mean in 2017	Relative increase from Pre-industrial level			
Carbon dioxide	About 278 ppm	405.5 ppm	+ 46 %	+2.2 ppm	+0.55 %	-
Methane	About 722 ppb	1,859 ppb	+157 %	+7 ppb	+0.38 %	12.4 years
Nitrous oxide	About 270 ppb	329.9 ppb	+ 22 %	+0.9 ppb	+0.27 %	121 years

28 Information on greenhouse gas monitoring is published on JMA's website.
https://www.data.jma.go.jp/ghg/info_ghg_e.html (Atmospheric greenhouse gases)
https://www.data.jma.go.jp/gmd/kaiyou/english/oceanic_carbon_cycle_index.html

29 See the WDCGG website for more information.
https://gaw.kishou.go.jp/

30 Data on the annual mean mole fraction in 2017 and its absolute and relative differences from the previous year are from WMO (2018b), while data on pre-industrial levels and lifetime are from IPCC (2013). The lifetime of gas as referred to here describes the time scale over which a local instantaneous increment of gas decays. The increase from pre-industrial levels is calculated from mole fractions for the pre-industrial era and 2017.

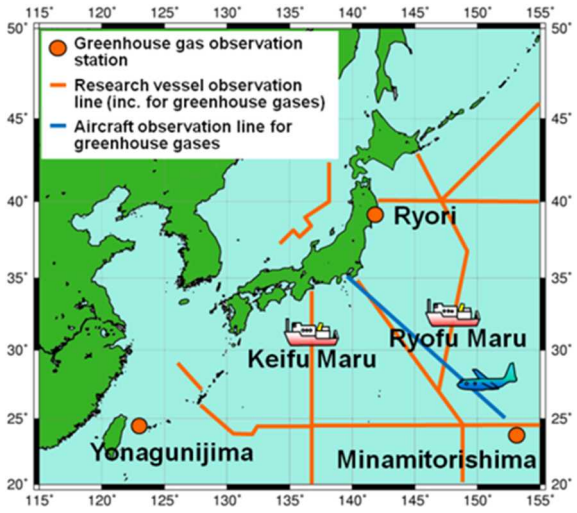

Figure 3.1-1 JMA's greenhouse gas observation network
Observation stations at Ryori, Minamitorishima and Yonagunijima and regular monitoring routes of research vessel and cargo aircraft

3.1.1 Concentration of carbon dioxide

(1) Concentration of global atmospheric carbon dioxide

The global mean concentration of atmospheric CO_2 shows a trend of increase with ongoing seasonal variations (Figure 3.1-2), primarily due to influences associated with human activity such as fossil fuel combustion and deforestation. Some anthropogenic CO_2 is absorbed by the terrestrial biosphere and the oceans, while the rest remains in the atmosphere. As most major sources of CO_2 are located in the Northern Hemisphere, concentrations tend to be higher in the mid- and high latitudes there and lower in the Southern Hemisphere (Figure 3.1-3).

The seasonal variability of CO_2 concentration is generally attributable to terrestrial biosphere activity. In summer, active plant photosynthesis consumes masses of CO_2, while emissions from plant respiration and organic-matter decomposition become dominant in winter. As a result, the annual maximum concentration is observed from March to April in the Northern Hemisphere and from September to October in the Southern Hemisphere. Seasonal variations exhibit larger amplitudes in the mid- and high latitudes of the Northern Hemisphere than in the ocean-rich Southern Hemisphere (Figure 3.1-3). Accordingly, the global mean CO_2 concentration usually peaks around April, reflecting the seasonal variations of the Northern Hemisphere.

WDCGG analysis shows that the global mean CO_2 concentration increased by 2.2 ppm from 2016 to 2017, reaching as much as 405.5 ppm (Table 3.1-1). The most recent 10-year average annual growth rate is 2.2 ppm/year, as opposed to the corresponding value of 1.5 ppm/year for the 1990s.

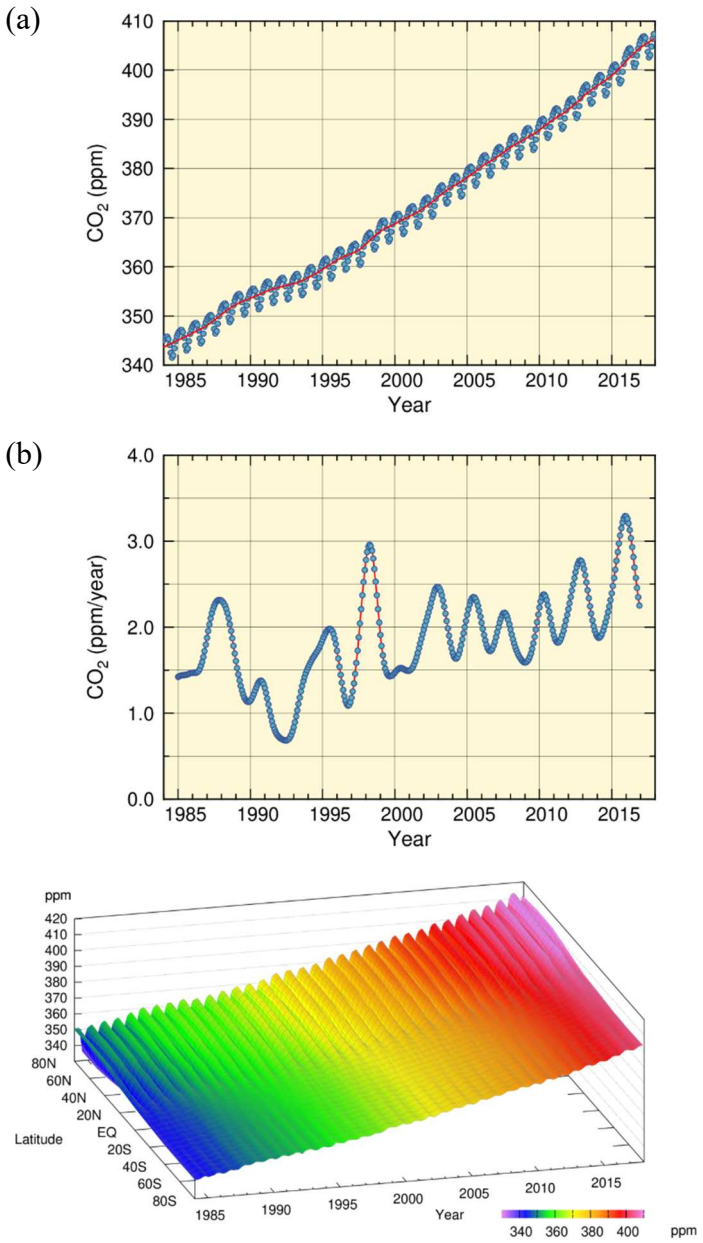

Figure 3.1-2 Global mean concentration of atmospheric CO_2 (a) and annual growth rate (b)

In the upper panel the blue dots are monthly values, and the red line represents the corresponding sequence after removal of seasonal variations. From the latter, the growth rate is derived and shown in the lower panel. Graph content is based on analysis of observation data reported to WDCGG using the method of WMO (2009). Data contributors are listed in WMO (2019).

Figure 3.1-3 Latitudinal distribution of atmospheric CO_2 concentrations

The data set and analysis method are as per Figure 3.1-2.

The growth rate of CO_2 concentration exhibits significant interannual variations (Figure 3.1-2 (b)). Major increases in concentration often coincide with El Niño events, largely because the terrestrial biosphere emits more CO_2 than usual under such conditions. In particular, El Niño events bring about high temperatures and droughts in tropical areas and elsewhere, thereby promoting plant respiration and organic-matter decomposition in soil and hindering plant photosynthesis (Keeling *et al.*, 1995; Dettinger and Ghil, 1998).

Figure 3.1-4 illustrates net CO_2 uptake by the terrestrial biosphere as estimated using the method of Le Quéré *et al.* (2016). Here, CO_2 uptake is defined as the amount of anthropogenic emissions minus the increment of atmospheric concentration and the amount of uptake by oceans. The low uptake by the terrestrial biosphere in 2015 and 2016 is generally attributed to the 2014 – 2016 El Niño event (WMO, 2018b). The annual net CO_2 uptake in 2015 and 2016 was 2.1 ± 1.0 GtC/year and 1.8 ± 1.1 GtC/year, respectively, both of which were lower than the 10-year average of 3.4 ± 1.0 GtC/year for the period 2006 – 2015. Similar suppression of net CO_2 uptake was observed in association with the El Niño events of 1997/1998 and 2002/2003. In 1998 in

particular, the lowest net uptake since 1990 was recorded. An exception was observed from 1991 to 1992, when net CO_2 uptake by the terrestrial biosphere was large despite the presence of an El Niño event. This is attributable to the eruption of Mt. Pinatubo in June 1991, which triggered worldwide low temperatures and inhibited CO_2 emissions from organic-matter decomposition in soil (Keeling *et al*., 1996; Rayner *et al*., 1999).

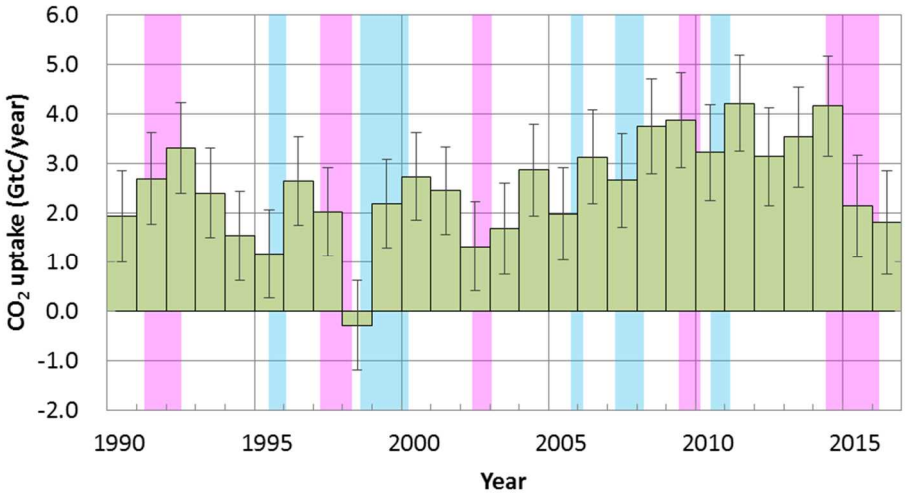

Figure 3.1-4 Annual net CO_2 uptake by the terrestrial biosphere
In this analysis, the net CO_2 uptake is estimated by subtracting the annual increment of atmospheric CO_2 and the amount of uptake by oceans from the amount of anthropogenic emissions. The amount of anthropogenic emissions, stemming from fossil fuel combustion and land-use changes, is based on Le Quéré *et al*. (2018). The annual increment of atmospheric CO_2 is the annual mean of the monthly means shown in Figure 3.1-2 (b). Oceanic uptake is based on Iida *et al*. (2015; see also Section 3.1.1 (3)), and incorporates emissions associated with the natural carbon cycle, corresponding to 0.7 GtC/year (IPCC 2013). Error bars indicate 68% confidence levels. El Niño and La Niña periods are shaded in red and blue, respectively. A negative CO_2 uptake equates to an emission.

(2) Concentration of atmospheric carbon dioxide in Japan

Concentrations of atmospheric CO_2 at all three of Japan's observation stations have shown a continuous increase along with seasonal variations (Figure 3.1-5 (a)). The amplitude of these variations is greater at Ryori than at the other stations because it tends to be larger in higher latitudes of the Northern Hemisphere in association with significant seasonal variations in terrestrial biosphere activity in the mid- and high latitudes (see Figure 3.1-1). Although Yonagunijima and Minamitorishima have similar latitudes, the former tends to observe higher concentrations and seasonal variations with larger amplitudes because of its greater proximity to the Asian continent, which is characterized by major anthropogenic emissions and an extensive biosphere. The annual mean CO_2 concentration in 2018 was 412.0 ppm at Ryori, 409.4 ppm at Minamitorishima and 411.7 ppm at Yonagunijima. All these figures are the highest on record (based on preliminary estimations).

Figure 3.1-5 (b) shows growth rates of CO_2 concentrations observed at the three observation stations. High rates have been observed in most cases during the periods of El Niño events. As a recent example, a sharp increase in CO_2 concentration was observed in association with the event that ran from summer 2014 to spring 2016.

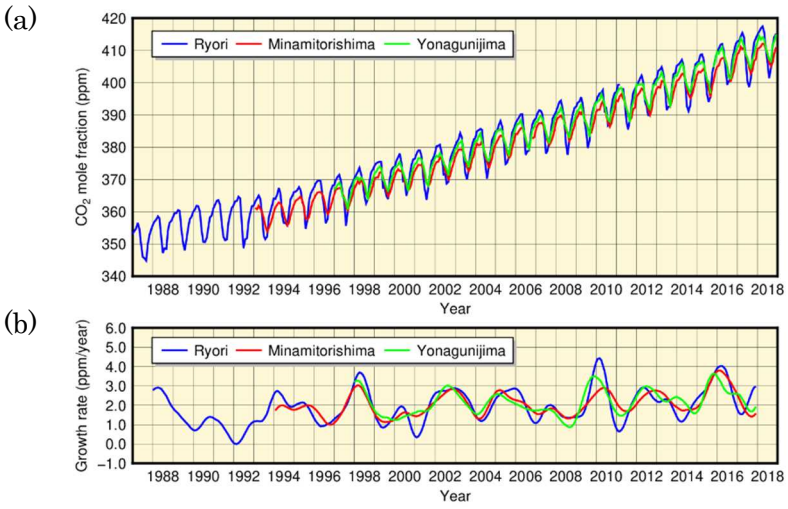

Figure 3.1-5 Monthly mean concentrations (a) and corresponding growth rates (b) of atmospheric CO_2 observed at Ryori (blue), Minamitorishima (red) and Yonagunijima (green)

The method used to calculate the growth rate is described in WMO (2009).

(3) Oceanic carbon dioxide

Based on data collected by JMA research vessels along the 137°E (3 – 34°N) and 165°E (5°S – 35°N) lines, oceanic and atmospheric pCO_2 are increasing in the western North Pacific area (Figures 3.1-6, 3.1-7). The growth rates for oceanic and atmospheric pCO_2 along the 137°E line from 1985 to 2018 were 1.4 – 2.1 and 1.7 – 1.9 µatm/year, respectively, while those along the 165°E line from 1996 to 2018 were 1.6 – 3.0 and 1.8 – 2.1 µatm/year, respectively. Oceanic pCO_2 exhibits seasonal variations, being higher in summer with higher SSTs and lower in winter with lower SSTs, and the range of variation is more volatile at higher latitudes along both lines. Meanwhile, atmospheric pCO_2 is constant and higher than those of oceanic pCO_2 except in summer. Consequently, the ocean absorbs atmospheric CO_2 emissions overall, other than in equatorial areas, resulting in a release of CO_2 into the atmosphere over the year because oceanic pCO_2 values are higher than those of atmospheric pCO_2.

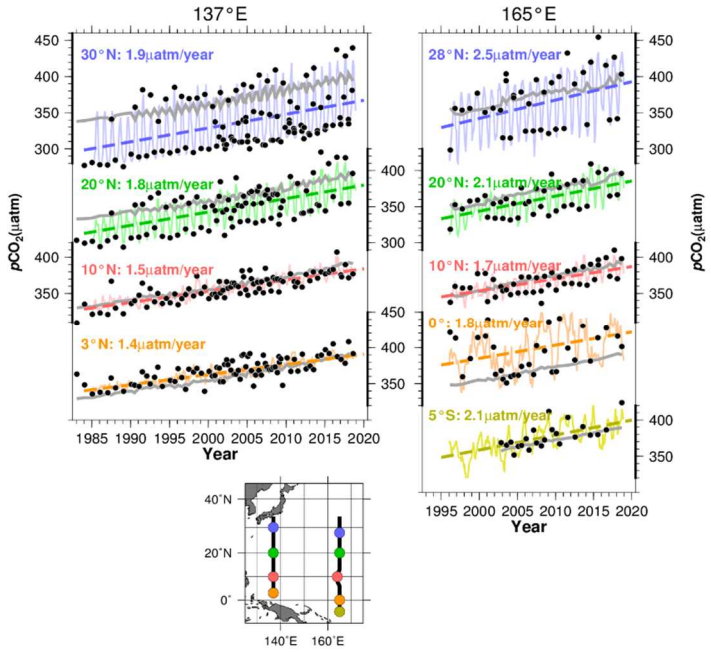

Figure 3.1-6 Annual changes in oceanic and atmospheric pCO_2 along the 137°E (left) and the 165°E (right) lines.

Black plots show oceanic pCO_2 observation values. Solid lines represent monthly oceanic pCO_2 values reconstructed using the method of Ishii et al. (2011), dashed lines show the long-term trend of oceanic pCO_2, and gray lines indicate the observed values of atmospheric pCO_2.

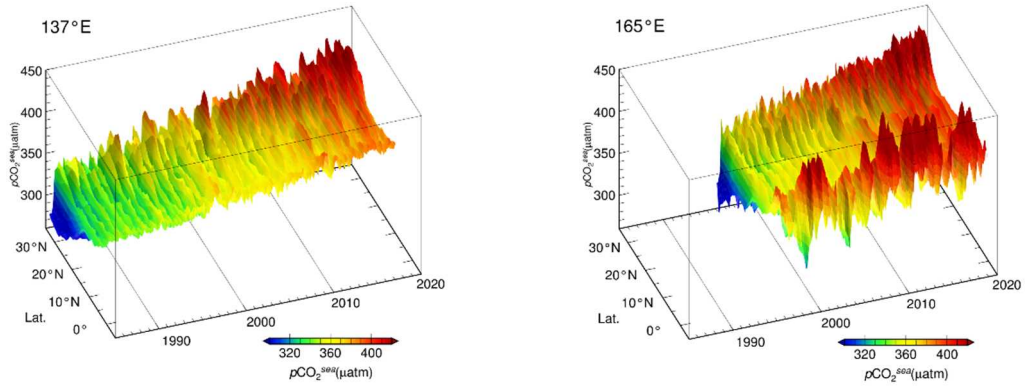

Figure 3.1-7 Time-latitude distribution of oceanic pCO2 along the 137°E (left) and the 165°E (right) lines.

Colors indicate reconstructed monthly oceanic pCO2 value. The part on the left shows oceanic pCO2 along the 137°E (3-34°N) since 1985 and the part on the right shows oceanic pCO2 along the 165°E (5°S-35°N) since 1996.

Analysis of observation data reveals relationships between surface seawater CO_2 concentrations and other oceanographic parameters such as sea surface temperature (SST), salinity and chlorophyll-a concentration, which differ by region. Global oceanic CO_2 concentrations were estimated using datasets of such parameters based on these relationships, and CO_2 exchanges between the atmosphere and the ocean were calculated (Iida *et al.*, 2015). It was found that the ocean releases CO_2 into the atmosphere in equatorial regions and the northern Indian Ocean, where seawater with a high CO_2 concentration upwells and absorbs CO_2 in other regions (Figure 3.1-8 (a)). Lower SSTs in winter and biological CO_2 consumption in spring/autumn result in lower surface ocean CO_2 concentrations and therefore higher CO_2 uptake, especially in the mid-to-high latitudes. Figure 3.1-8 (b) and (c) show monthly and annual variations in global ocean CO_2 uptake, respectively. The estimated mean annual global ocean CO_2 uptake during 1990 to 2017 was 1.8 GtC per year. Considering natural CO_2 efflux of 0.7 GtC per year (IPCC, 2013), which results from riverine input to the oceans, the amount of oceanic CO_2 uptake corresponds to 30 % of all anthropogenic CO_2 emission, which IPCC (2013) estimates to be 9 GtC per year. Global ocean CO_2 uptake is affected by the variability of global SST distribution and biological activity, and decreases/increases in boreal summer/winter (Figure 3.1-8 (b)). The estimated annual global ocean CO_2 uptake has increased since 2000.

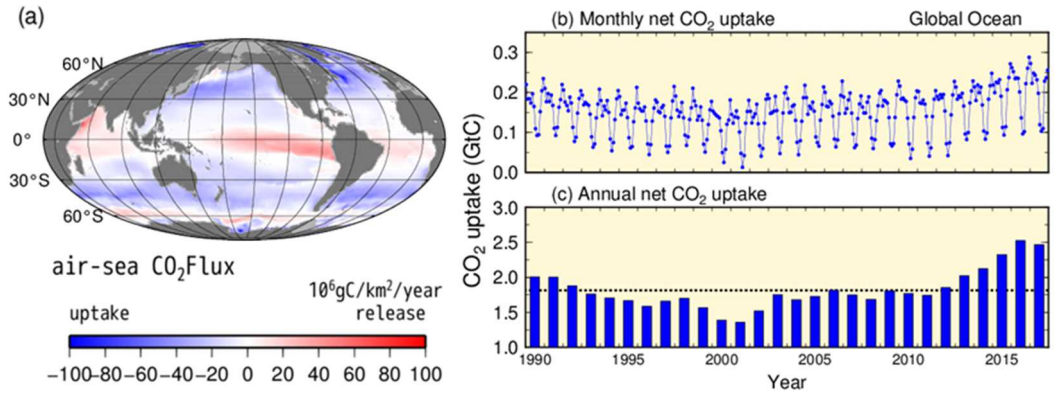

Figure 3.1-8 Distribution of global ocean CO_2 uptake/release for 2017 (a) and time-series representations of monthly (b) and annual (c) CO_2 uptake from 1990 to 2017

The blue/red area in the map on the left (a) indicates ocean uptake/release of CO_2 from/into the atmosphere. The grey area shows the border of the region analyzed. The dotted line in graph (c) shows the 1.8 GtC average for the period from 1990 to 2017.

The column inventory of oceanic CO_2 was estimated using long-term time-series data on dissolved inorganic carbon from 1990s (Figure. 3.1-9). The column inventory rates of oceanic CO_2 between the sea surface and 27.5 σ_θ (1,200 to 1,400 m in depth) along 137°E and 165°E are approximately 5 – 12 and 3 – 12 $tC \cdot km^{-2} \cdot year^{-1}$, respectively. The column inventory rates of oceanic CO_2 around 20 – 30°N are higher than those at 10°N and 35°N. This is caused by the transport of CO_2 from the surface to the ocean interior by water masses known as North Pacific subtropical mode water and North Pacific intermediate water.

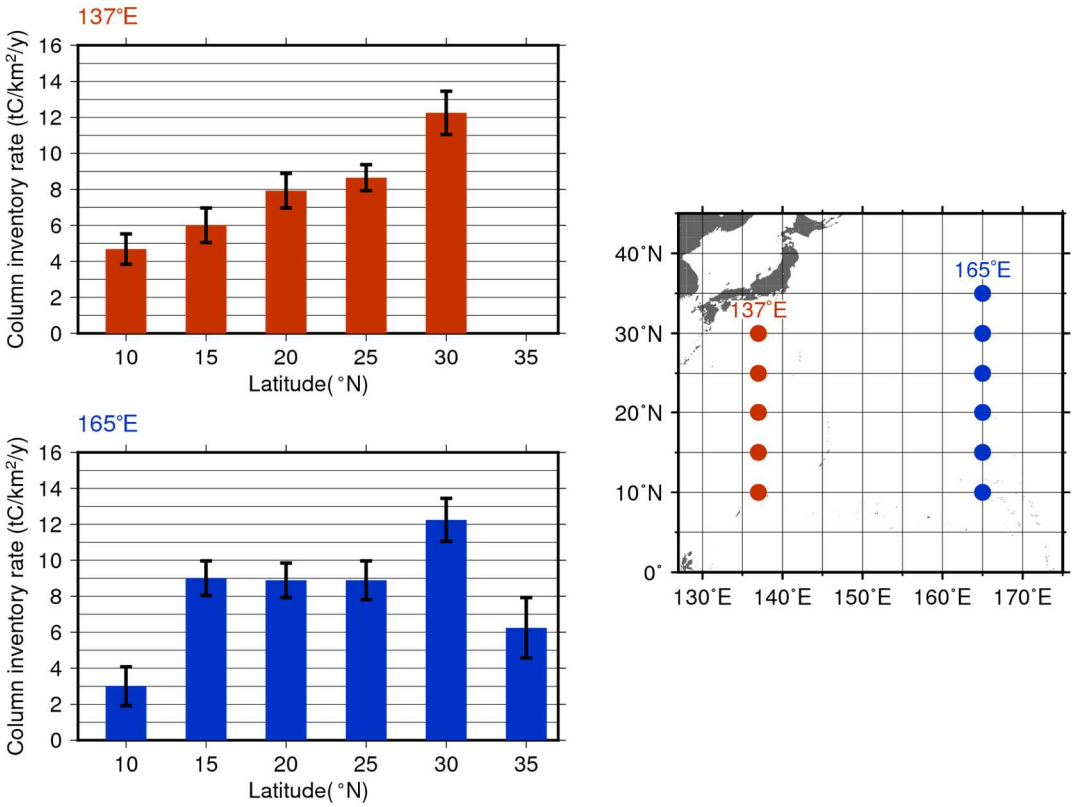

Figure 3.1-9 Changes in oceanic CO_2 between the sea surface and 27.5 σ_θ (approx. 1,200 – 1,400 m in depth) along 137 and 165°E for the periods 1994 – 2018 and 1992 – 2018.

Error bars denote a 95% confidence level

(4) Ocean acidification

The ocean acts as a large sink for CO_2 emitted as a result of human activity, and the chemical properties of seawater have changed due to the uptake and reserve of anthropogenic CO_2. Ocean acidification, known as the decrease in seawater pH (hydrogen ion exponents), is a particular issue of concern because it accelerates global warming by limiting the ocean's capacity of CO_2 uptake from the atmosphere and affects marine ecosystems by disturbing plankton growth. The IPCC AR5 (2013) included an estimate that the average global surface seawater pH has decreased by 0.1 due to ocean uptake of atmospheric CO_2 emitted as a result of human activity since the beginning of the industrial era (1750). According to numerical model experiments based on future CO_2 emission estimates, surface seawater pH will further decease by 0.065 – 0.31 by the end of 21st century. The CO_2 absorbed by the ocean is considered to have been transported into the ocean interior through ocean circulation and biological processes, and to be causing ocean acidification in the interior as well as in the surface layer (Doney et al., 2009).

JMA has long conducted oceanographic observations in the western North Pacific to monitor long-term variability relating to the ocean, such as global warming and ocean acidification. The Agency monitor long-term trends in surface and interior seawater pH along repeat hydrographic lines at 137°E and 165°E, and performs analysis to determine the average decrease in surface seawater pH throughout the Pacific using data on oceanic CO_2 concentration and related factors. The results clearly show a decreasing trend in surface seawater pH for the whole Pacific, and 0.013 to 0.021 and 0.014 to 0.031 per decade at individual stations on the 137°E and 165°E lines, respectively (Figures 3.1-10 and 3.1-11). Ocean interior pH along these lines also shows decreasing trends of 0.011 to 0.035 per decade (Figure 3.1-12) with higher rates in the northern than the southern subtropics due to greater accumulation of anthropogenic CO_2 in the former.

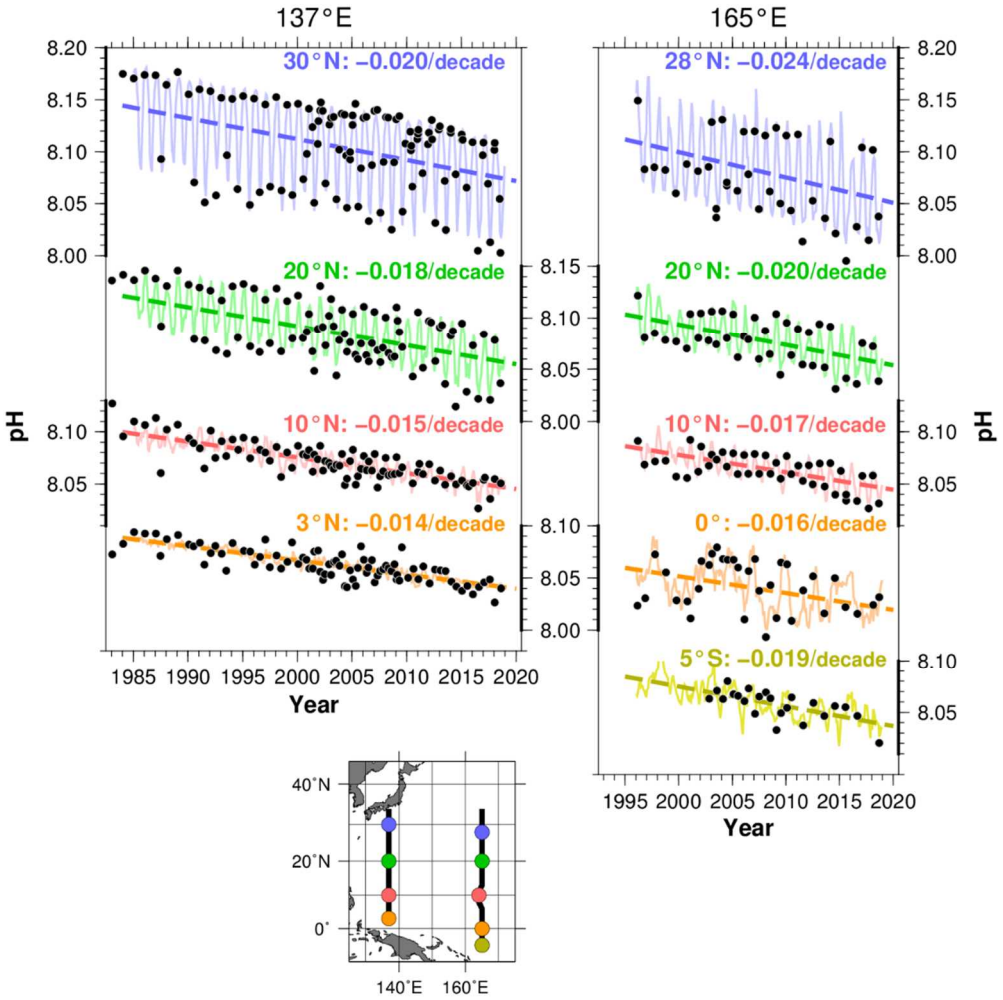

Figure 3.1-10 Long-term trends of pH at each latitude in JMA's repeat hydrographic lines at 137°E (left) and 165°E (right).

Black plots show pH observation values based on pCO_2 observation data. Solid lines represent monthly pH values reconstructed using the method of Ishii et al. (2011), dashed lines show the long-term trend of pH, and numbers indicate rates of change at each latitude.

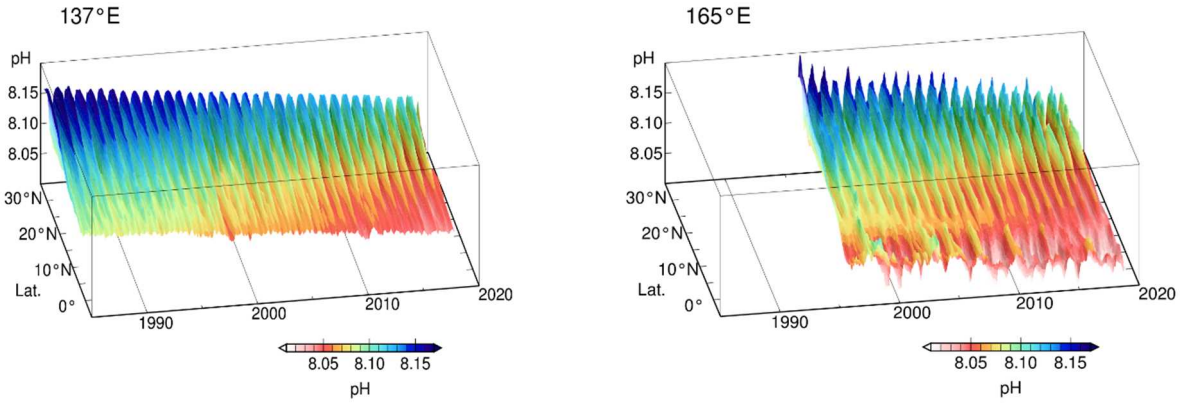

Figure 3.1-11 Time-latitude distribution of pH along the 137°E (left) and the 165°E (right) lines.

Colors indicate reconstructed monthly pH values. The part on the left shows pH along 137°E (3-34°N) since 1985, and the part on the right shows pH along 165°E (5°S-35°N) since 1996.

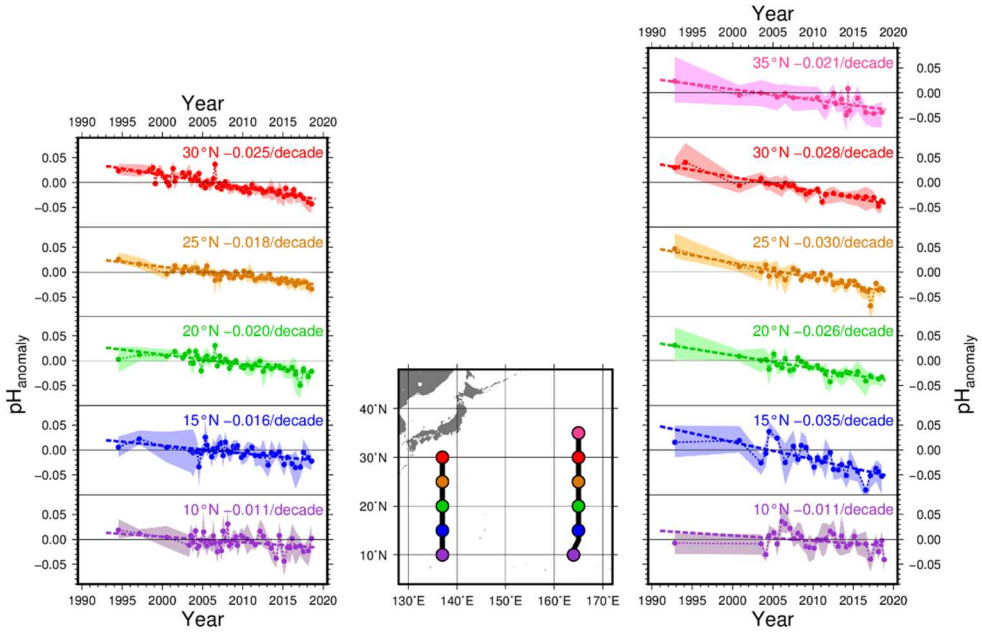

Figure 3.1-12 Long-term trends of pH between 25.0 σ_θ and 26.9 σ_θ (a depth range of about 150~800 m) along 137°E (left) and 165°E (right).

Plots show pH anomalies from the normal (i.e., the average for the period from 1991 to 2010) at each latitude. The shaded areas and bold dotted lines represent the standard deviation range (±1 σ) and the long-term trend, respectively. The numbers indicate rates of change at each latitude.

(5) Concentration of carbon dioxide in the upper air

Since 2011, JMA has monitored upper-air CO_2 concentrations using cargo aircraft with support from Japan Ministry of Defense, with air samples taken along the route from Atsugi Air Base (35.45°N, 139.45°E) to Minamitorishima Island (24.29°N, 153.98°E) during level flight at an altitude of approximately 6 km and during descent to the island once a month (Tsuboi *et al*., 2013; Niwa *et al*., 2014).

Figure 3-1.13 shows measured and averaged concentrations for samples collected during level flight in black and blue dots, respectively. Monthly mean concentrations at the ground-based station on the island are also shown in red. The dashed curves in blue and red represent components after removal of seasonal cycles for aircraft and Minamitorishima, respectively. Concentrations exhibit a gradual increase over time in the upper air as well as on the surface, although values tend to be lower in the former.

At ground level on the island, concentrations are higher from winter to spring and lower from summer to fall. Those in the upper air tend to be lower than on the surface during winter to spring, while similar values are observed for the corresponding altitudes in summer. Consequently, the amplitude of seasonal cycles is smaller in the upper air shown in Figure 3-1.14. The Figure shows the vertical dependence of average seasonal cycles based on air samples collected during descent in addition to level-flight data and ground-based data. From winter to spring, concentrations are lower toward higher altitudes.

Figure 3-1.15 shows concentrations for samples taken during descent minus the daily mean value recorded at the ground-based station on the flight date for February (left) and August (right). While concentrations are lower toward higher altitudes in February, there is no clear vertical

dependence in August.

The above results suggest that parts of surface air affected by the terrestrial biosphere in continental regions are transported to the ground and upper levels of the island, and that air transport behavior varies with seasons and altitudes. The characteristic of strong vertical dependence from winter to spring and weak dependence from summer to fall is also identified in data from other aircraft observations around North America and Asia (Sweeney *et al*., 2015; Umezawa *et al*., 2018).

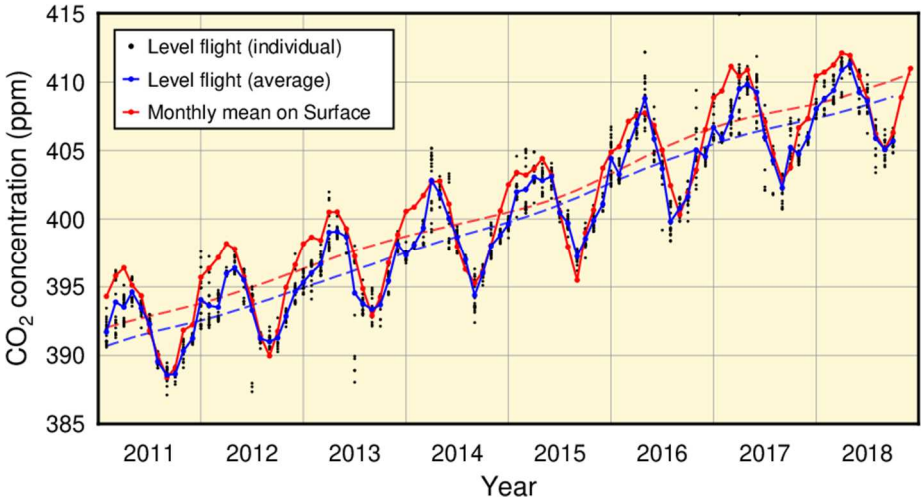

Figure 3.1-13 Measured and averaged CO_2 concentrations for air samples collected during level flight (at a height of approx. 6 km) of cargo aircraft along the route from Atsugi Air Base to Minamitorishima (black and blue dots, respectively) and monthly mean concentrations at the Minamitorishima ground-based station (red dots).

Blue and red dashed curves represent the component after removal of seasonal cycles from the series of red and blue dots, respectively. The analysis is based on WMO (2009).

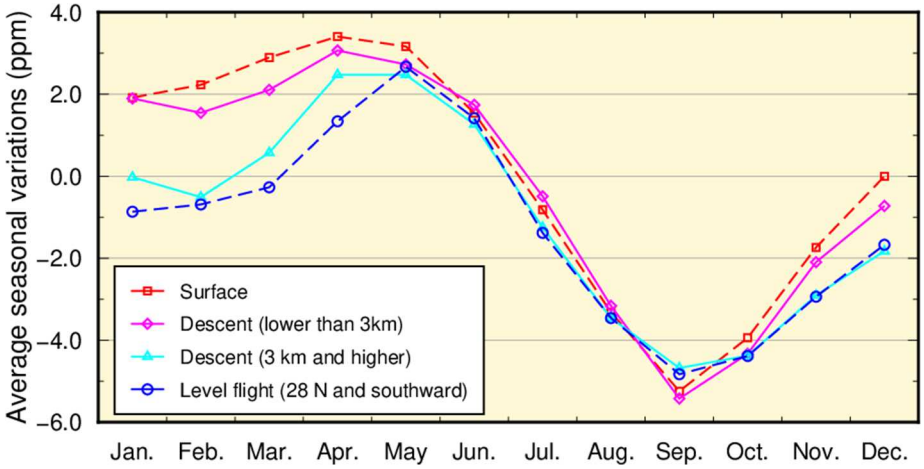

Figure 3.1-14 Vertical dependence of average seasonal cycles around Minamitorishima for monthly mean concentrations on the surface (red), concentrations for air samples taken during level flight at latitudes 28°N and southward (blue), and those taken during descent with altitudes less than 3 km (magenta) and otherwise (cyan).

Monthly values are calculated by averaging concentrations after the removal of long-term trends (components without seasonal cycles) of surface data.

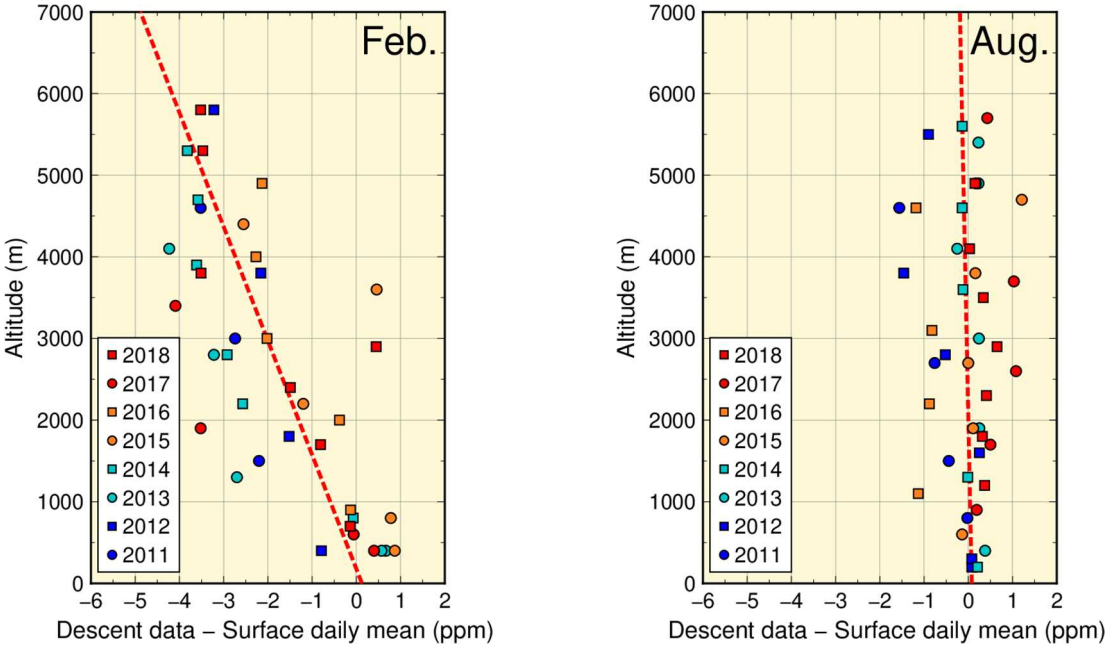

Figure 3.1-15 Vertical variations of CO_2 concentrations over Minamitorishima
Circles and squares show concentrations of air samples taken during descent to the island minus the daily mean value recorded at the ground-based station on the flight date. Symbol colors and shapes represent observation years. Dashed red lines show the vertical gradient of the symbols as determined using the least squares method.

3.1.2 Concentration of methane

(1) Concentration of global atmospheric methane

The global mean concentration of atmospheric CH_4 has been increasing since at least the mid-1980s when worldwide monitoring began, except for a stationary phase from 1999 to 2006 (Figure 3.1-16). The mechanism behind the stationary phase remains unclear, but several scenarios have been proposed (IPCC, 2013). The greater concentrations observed since 2007 indicate an increase in CH_4 emissions from tropical wetlands and human activity in the mid-latitudes of the Northern Hemisphere (WMO, 2018b).

WDCGG analysis shows that the global mean concentration of CH_4 in 2017 was 1,859 ppb, which is the highest since records began (Table 3.1-1).

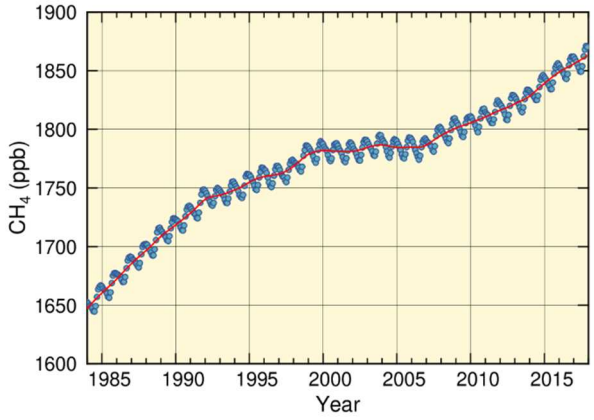

Figure 3.1-16 Global mean concentration of atmospheric CH_4

The blue dots are monthly values, and the red line represents the corresponding sequence after the removal of seasonal variations. Graph content is based on analysis of observation data reported to WDCGG based on the method of WMO (2009). Data contributors are listed in WMO (2019).

Figure 3.1-17 shows the latitudinal dependence of CH_4 concentrations. In the high and mid-latitudes of the Northern Hemisphere, concentrations begin to sharply decrease toward the south. This is because CH_4 is mostly emitted from land areas in the Northern Hemisphere, and disappears due to reaction with hydroxyl radicals[31] over tropical oceans during transportation to the Southern Hemisphere. In summer, more hydroxyl radicals are produced as a result of enhanced ultraviolet radiation, and a larger amount of CH_4 is destroyed. This reaction creates seasonal variation of CH_4 concentrations, as seen in Figures 3.1-16 and 3.1-17.

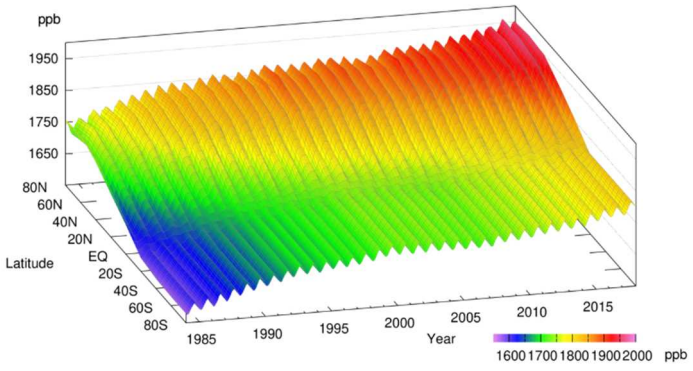

Figure 3.1-17 Latitudinal distribution of atmospheric CH_4 concentrations

The data set and analysis method are as per Figure 3.1-16.

31 Hydroxyl radicals are highly reactive chemicals generated by the reaction of atomic oxygen, which is derived from UV photolysis of ozone, with airborne water vapor. It is particularly abundant at low latitudes, where UV radiation is strong and water vapor is plentiful.

The remarkable increase observed in global mean atmospheric concentrations of CH_4 since the industrial era (+157%) has been much more rapid than that of CO_2 (+46%) (Table 3.1-1). This is partly because the amount of anthropogenic emissions of CH_4 relative to natural emissions exceeds that of CO_2. The long-term trend of CH_4 concentration depends on various factors of uncertainty, including anthropogenic/natural emissions and chemical reactions. Accordingly, further development of the global CH_4 observation network is required.

(2) Concentration of atmospheric methane in Japan

Atmospheric CH_4 concentrations at all of Japan's three observation stations exhibit a trend of increase with seasonal variations in the same way as the global mean concentration (Figure 3.1-18 (a)). Ryori usually observes the highest concentration among the three stations because it is located in the northern part of Japan, where CH_4 sources in the Asian continent are more influential and reaction with hydroxyl radicals is less marked. Although Yonagunijima and Minamitorishima are located at similar latitudes, the former tends to record higher concentrations in winter because CH_4 sources on the Asian continent have a stronger impact there in winter as a result of continental air mass expansion. In summer, meanwhile, a hydroxyl radical-rich maritime air mass covers both stations, and similarly low concentrations are observed. Since 2010, Yonagunijima has occasionally observed concentrations as high as those of Ryori in winter. The annual mean CH_4 concentration in 2018 was 1,941 ppb at Ryori, 1,893 ppb at Minamitorishima and 1,915 ppb at Yonagunijima, all of which are the highest on record (based on preliminary estimations).

The growth rate of atmospheric CH_4 concentration exhibits interannual variations that differ significantly from station to station (Figure 3.1-18 (b)).

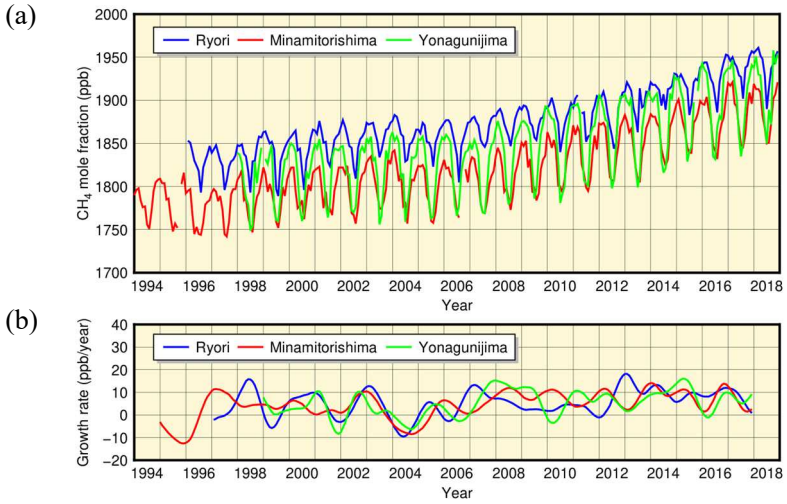

Figure 3.1-18 Monthly mean concentrations (a) and corresponding growth rates (b) of atmospheric CH_4 observed at Ryori (blue), Minamitorishima (red) and Yonagunijima (green)

The method for calculating the growth rate is described in WMO (2009).

3.1.3 Concentration of nitrous oxide

Figure 3.1-19 shows that the global mean concentration of atmospheric N_2O has been continuously increasing with small seasonal variations, in contrast to the situations with CO_2 and CH_4. The annual mean concentration in 2017 was 329.9 ppb, which was 22% above the pre-industrial level of 270 ppb (Table 3.1-1). The hemispheric mean concentration is approximately 1 ppb higher in the Northern Hemisphere than in the Southern Hemisphere (Figure 3.1-20) because there are more sources of anthropogenic and soil emissions in the former. This interhemispheric difference is, however, much smaller than those observed with CO_2 and CH_4.

The atmospheric N_2O concentration at Ryori exhibits characteristics similar to those of the global mean (Figure 3.1-21). The annual mean concentration in 2018 at Ryori was 332.7 ppb (based on preliminary estimations).

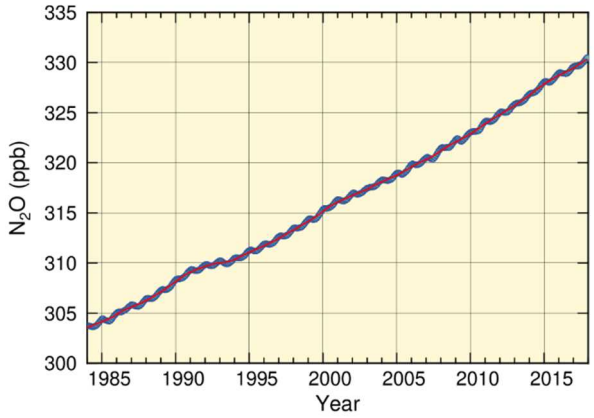

Figure 3.1-19 Global mean concentration of atmospheric N_2O

The blue dots are monthly values, and the red line represents the corresponding sequence after the removal of seasonal variations. Graph content is based on analysis of observation data reported to WDCGG based on the method of WMO (2009). Data contributors are listed in WMO (2019).

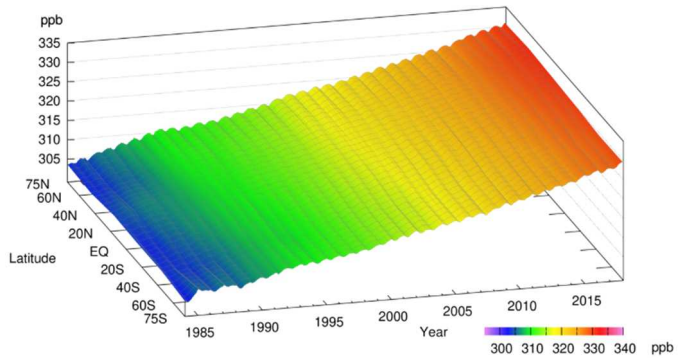

Figure 3.1-20 Latitudinal distribution of atmospheric N_2O concentrations

The data set and analysis method are as per Figure 3.1-19.

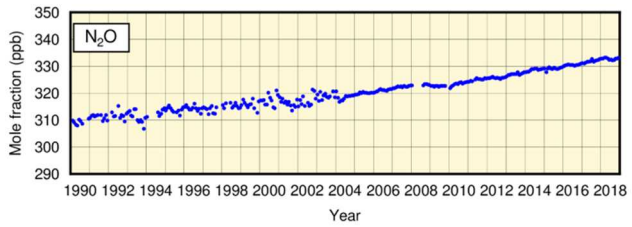

Figure 3.1-21 Monthly mean concentrations of atmospheric N_2O at Ryori

Improvement of observation equipment in 2004 resulted in improved stability of measurements.

3.2 Monitoring of the ozone layer and ultraviolet radiation[32]

- ○ Global-averaged total ozone amount decreased significantly in the 1980s and the early 1990s, and remains low today with a slightly increasing trend.
- ○ The annual maximum area of the ozone hole in the Southern Hemisphere increased substantially in the 1980s and 1990s, but a statistically significant decreasing trend since 2000 has been identified.
- ○ UV radiation levels at three domestic sites have increased since the early 1990s. Annual cumulative daily erythemal UV radiation at Tsukuba is virtually certain to have increased for the whole of the observational period at a rate of 4.5% per decade.
- ○ Global atmospheric concentrations of chlorofluorocarbons (CFCs) have gradually decreased in recent years.

JMA monitors total ozone and/or vertical profiles of ozone at three domestic sites and one Antarctic site (Sapporo, Tsukuba, Naha and Syowa Station) under the Act on the Protection of the Ozone Layer through the Control of Specified Substances and Other Measures[33]. It also monitors ultraviolet radiation at Tsukuba and Syowa. JMA also monitors the surface concentration of CFCs at Ryori (Figure 3.2-1).

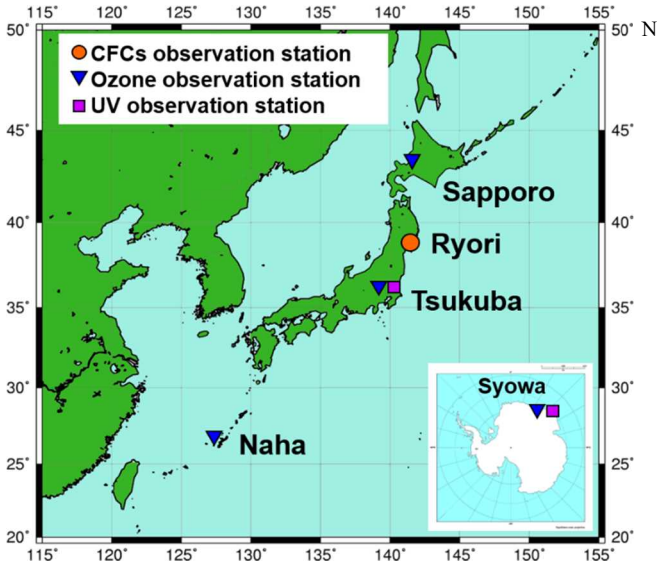

Figure 3.2-1 JMA's ozone layer and ultraviolet radiation observation network

3.2.1 Ozone layer

(1) Global ozone layer

Globally averaged total ozone amount decreased considerably in the 1980s and the early 1990s (Figure 3.2-2). Although uniformity or a slightly increasing trend has been observed since the mid-1990s, total ozone levels have remained lower than those seen before the 1980s. Global mean total ozone with enough data points for statistical analysis for the period 2013 – 2017 was approximately 1% higher than the 1994 – 2008 mean and 3% lower than the 1970 – 1980 mean, which is a representative value for the period prior to the onset of ozone depletion. A report titled

32 Information on the ozone layer and ultraviolet radiation is published on JMA's website.
https://www.data.jma.go.jp/gmd/env/ozonehp/en/diag_o3uv_e.html

33 Law No. 53 of May 20, 1988, Article 22: Observation and monitoring
1. The Director-General of the Meteorological Agency shall observe the state of the ozone layer and the atmospheric concentrations of specified substances and publish the results obtained.

Scientific Assessment of Ozone Depletion: 2018 (WMO, 2018a) stated that action taken under the Montreal Protocol has led to a reduction in the atmospheric abundance of controlled ozone-depleting substances (ODSs), and that upper-stratospheric ozone have increased since 2000.

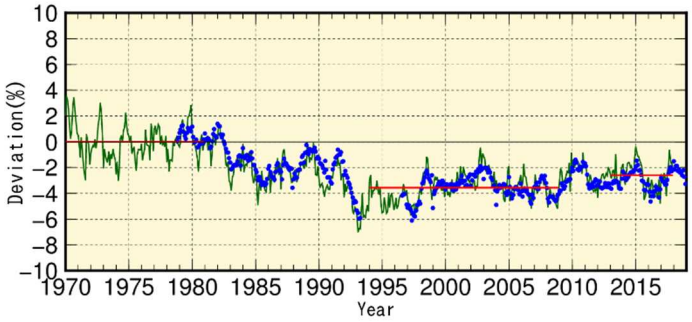

Figure 3.2-2 Time-series representation of global-averaged total ozone deviations shown as percentages
The green line represents deviations of monthly mean global-area-weighted total ozone from the 1970 – 1980 mean, the three red lines represent the 1970 – 1980 mean, the 1994 – 2008 mean and the mean over the last five years when there were enough data points for a statistical analysis (2013 – 2017), and the blue dots show NASA TOMS/OMI satellite data averaged at latitudes of 70°S – 70°N. Each data set is deseasonalized with respect to the whole observation period. A total of 114 ground-based stations were used for this calculation (91 in the Northern Hemisphere and 23 in the Southern Hemisphere).

(2) Antarctic ozone hole[34]

The annual maximum area of the ozone hole in 2018 exceeded the most recent decadal average due to very cold stratospheric conditions, but was smaller than those observed from the late 1990s to the early 2000s. The annual maximum area of the ozone hole in the Southern Hemisphere increased substantially in the 1980s and 1990s, but a statistically significant decreasing trend since 2000 has been identified as described in Topics II (The trend of Antarctic ozone layer recovery).

The annual ozone hole area depends on regional interannual climate variations, but also shows decadal variations in line with total amounts of ODSs in the stratosphere. A report titled *Scientific Assessment of Ozone Depletion: 2018* (WMO, 2018a) stated that the Antarctic ozone hole is expected to gradually close, with springtime total column ozone returning to 1980 values in the 2060s.

34 See the Glossary for terms relating to ozone hole.

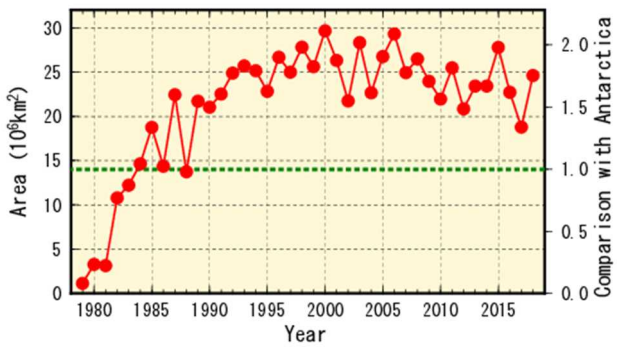

Figure 3.2-3 Time-series representation of the annual maximum ozone hole area

The ozone hole area is defined as the region over which total ozone south of 45°S is equal to or less than 220 m atm-cm. NASA TOMS/OMI and NOAA-TOVS satellite data are used in calculation of the area for 1979 – 2018. The green line indicates the overall area of the Antarctic (1.39×10^7 km^2). The left axis shows the ozone hole's maximum area in units of 10^6 km^2, and the right axis shows its ratio to the area of Antarctica itself.

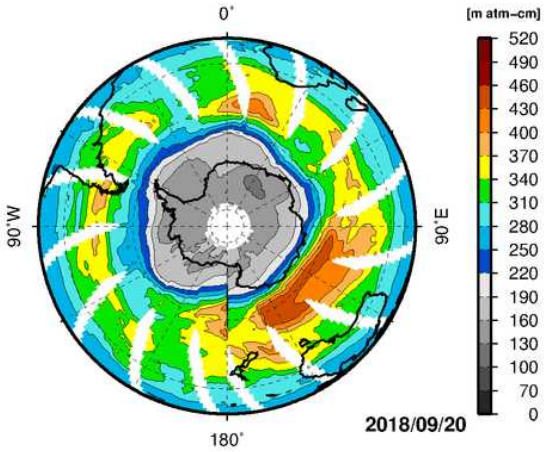

Figure 3.2-4 Southern Hemisphere distribution of total ozone on 20 September 2018, when the area of the ozone hole reached its maximum for the year

The unit is m atm-cm, and the map is produced using NASA OMI satellite data. The grey shading in the center shows ozone hole areas where the total ozone column value is 220 m atm-cm or less. White regions are domains where no satellite data were available.

(3) Ozone layer over Japan

Figure 3.2-5 shows time-series representations of annual-mean total ozone observed at Sapporo, Tsukuba and Naha. A decrease is seen in the 1980s and the early 1990s at Sapporo and Tsukuba. After 2000, slightly increasing trends are observed at all three sites, but an ongoing trend of relatively low values has been seen in recent years at Naha.

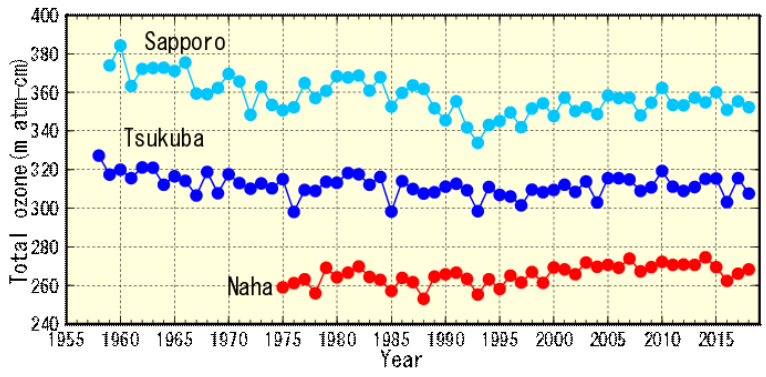

Figure 3.2-5 Time-series representations of annual-mean total ozone at stations in Japan

The stations here are at Sapporo, Tsukuba and Naha. JMA began observing total ozone at Tsukuba in 1957 and currently monitors total ozone and/or vertical profiles of ozone at three domestic sites (Sapporo, Tsukuba, Naha) and one Antarctic site (Syowa Station).

3.2.2 Solar UV radiation in Japan

UV radiation levels at three domestic sites have been increased from early-1990s. Annual cumulative daily erythemal UV radiation[35] at Tsukuba is virtually certain to have increased for the whole of the observational period by ratios of 4.5% per decade (Figure 3.2-6). At Sapporo, UV radiation levels increased from the mid-1990s to the 2000s. At Tsukuba, UV radiation levels increased in 1990s. At Naha, data show no marked changes since the increase observed in the 1990s. This phenomenon may be attributable to a decreasing tendency of aerosols and air pollution, and/or to changes in cloudiness and other meteorological conditions over monitoring sites (UNEP, 2015; JMA, 2011).

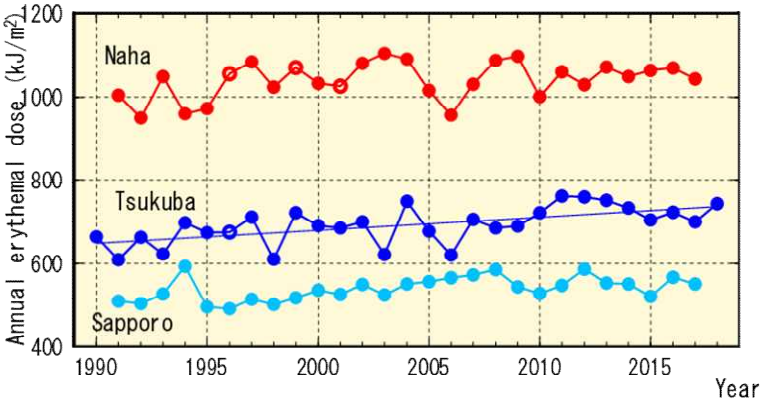

Figure 3.2-6 Time-series representations of annual cumulative daily erythemal UV radiation
Observation of erythemal UV at Sapporo, Tsukuba and Naha in Japan started in the early 1990s. Each annual cumulative total is calculated from monthly-mean equivalent values multiplied by the number of days in each month. The monthly-mean equivalent value is based on calculation using daily values from which missing data are excluded. Open circles represent cases of at least a month in which there are fewer than 20 days of monitoring data. Regression lines cover the whole observation period (statistically significant at a confidence level of 99% for Tsukuba). UV radiation observations at Sapporo and Naha were terminated in January 2018.

3.2.3 Concentration of ozone-depleting substances

Chlorofluorocarbons (CFCs: CFC-11, CFC-12 and CFC-113), which are compounds of carbon, fluorine and chlorine, and other halogenated gases are ozone-depleting substances (ODSs). They are regulated under the 1987 Montreal Protocol on Substances that Deplete the Ozone Layer and its Amendments and Adjustments. Although ODSs have atmospheric concentrations equivalent to about a millionth of CO_2 levels at most, they contribute considerably to global warming because of their significant radiative effects per unit mass, some of which are several thousand times greater than that of CO_2.

(1) Global concentration of ozone-depleting substances

Global concentrations of atmospheric CFCs increased rapidly until the 1980s before entering a decreasing trend in the 1990s (Figure 3.2-7). The concentration of CFC-11 peaked in 1992 – 1994, and has since shown a decreasing tendency. The concentration of CFC-12 increased until around 2003, and has also since shown a decreasing tendency. The concentration of CFC-113 reached its maximum in around 1993 in the Northern Hemisphere and around 1996 in the Southern Hemisphere. Differences in the concentrations of these gases between the Northern Hemisphere, where most emissions sources are located, and the Southern Hemisphere, which has significantly fewer sources, have decreased since the 1990s in contrast to the situation of the 1980s. These observations indicate that the CFC emission controls under the Montreal Protocol have been effective.

35 See the Glossary for terms relating to erythemal UV radiation.

However, a slowdown in the decline of CFC-11 concentrations has been observed since 2012 (WMO, 2018a; WMO, 2018b; Montzka *et al*., 2018), with decreasing rate approximately two thirds of those seen in the preceding decade. Numerical model calculation reporting by Montzka *et al*. (2018) attributed this to increased global CFC-11 emissions with main sources probably located in eastern Asia.

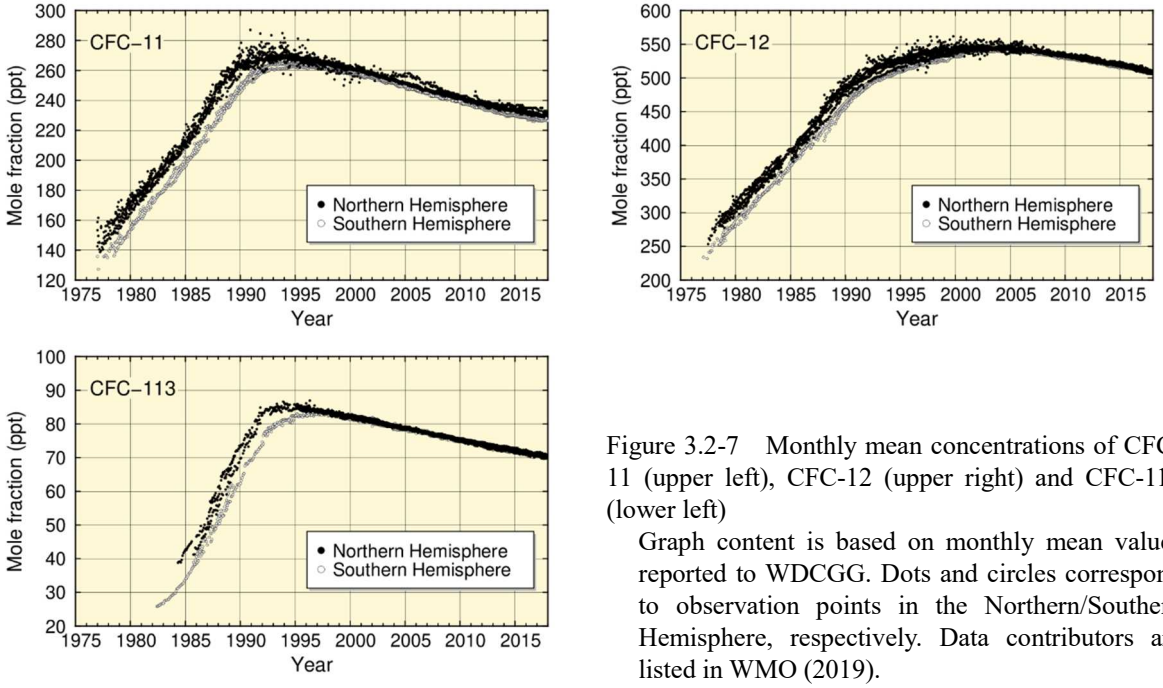

Figure 3.2-7 Monthly mean concentrations of CFC-11 (upper left), CFC-12 (upper right) and CFC-113 (lower left)
Graph content is based on monthly mean values reported to WDCGG. Dots and circles correspond to observation points in the Northern/Southern Hemisphere, respectively. Data contributors are listed in WMO (2019).

(2) Concentration of ozone-depleting substances in Japan

Concentrations of CFC-11, CFC-12 and CFC-113 at Ryori have shown decreasing tendencies since reaching maxima in various years (Figure 3.2-8). The concentration of CFC-11 peaked at about 270 ppt in 1993 – 1994, and has since decreased. The distinct peak of concentration observed in summer 2011 is considered attributable to emissions from polyurethane foam insulation materials released by the Great East Japan Earthquake and the subsequent hugely destructive tsunami of 11 March 2011 (Saito *et al*., 2015). The rate of increase in CFC-12 concentration slowed around 1995, and a gradual decrease has been seen since 2005. There was no clear tendency of increase or decrease in the concentration of CFC-113 until 2001, but a decreasing tendency has been seen since then.

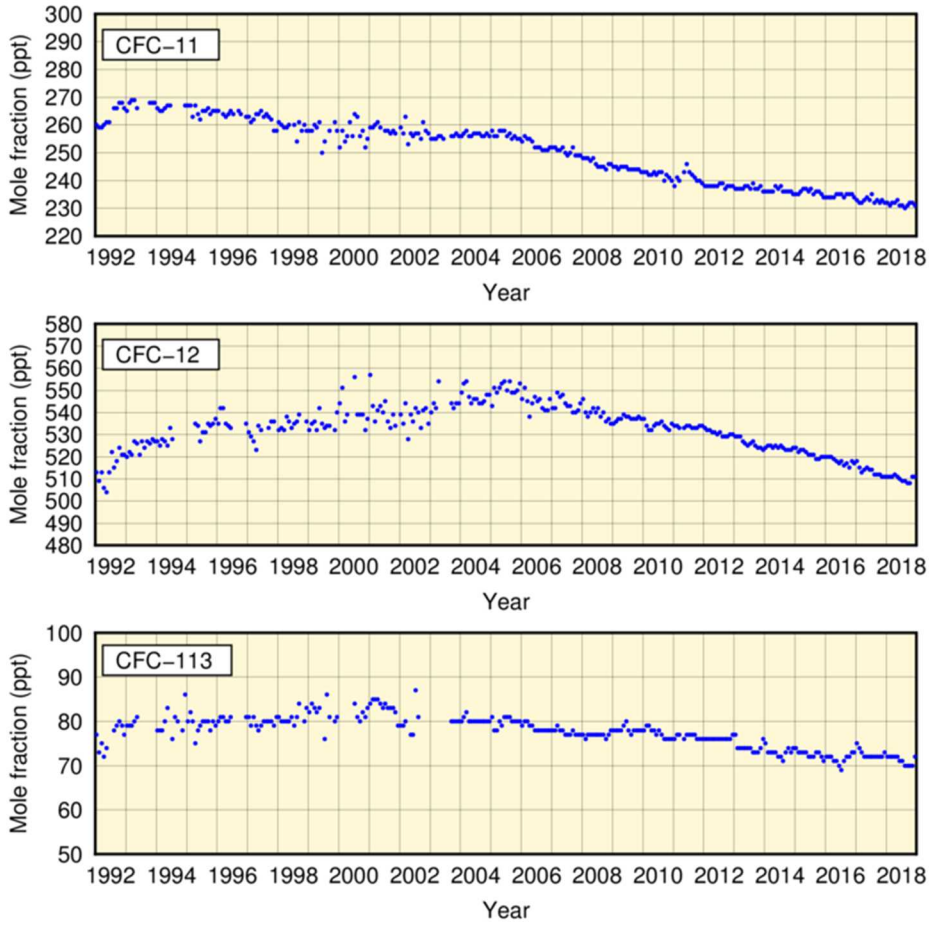

Figure 3.2-8 Monthly mean atmospheric concentrations of CFC-11 (top), CFC-12 (middle) and CFC-113 (bottom) at Ryori

Improvement of observation equipment in 2003 resulted in improved stability of measurements.

3.3 Monitoring of aerosols and surface radiation[36]

- ○ In Japan, background atmospheric turbidity coefficient values (which depend on concentrations of aerosols, water vapor and other constituents in the air) have returned to approximate levels seen before the eruption of Mt. Agung in 1963. This is mainly because of no large-scale eruptions impacting the global climate since that of Mt. Pinatubo in 1991.
- ○ The number of days when any meteorological station in Japan observed Kosa was 11 in 2018, and the total number of stations reporting its occurrence during the year was 104.

3.3.1 Aerosols

Interannual variations in the atmospheric turbidity coefficient[37], which is calculated from direct solar radiation[38] measurements taken at five stations in Japan excluding the fluctuation component of the troposphere, shows a clear impacts of stratospheric aerosols resulting from volcanic eruptions (Figure 3.3-1). The increased turbidity coefficients observed for several years after 1963 and during the periods of 1982 – 1983 and 1991 – 1993 were caused by the eruptions of Mt. Agung (Indonesia) in 1963, Mt. El Chichón (Mexico) in 1982 and Mt. Pinatubo (Philippines) in 1991, respectively. The increased turbidity stems from the persistent presence of sulfate aerosol in the stratosphere resulting from huge amounts of SO_2 released by the volcanic eruptions. The turbidity coefficient has now returned to approximately the same level as that observed before the eruption of Mt. Agung because no large-scale eruptions have occurred since that of Mt. Pinatubo.

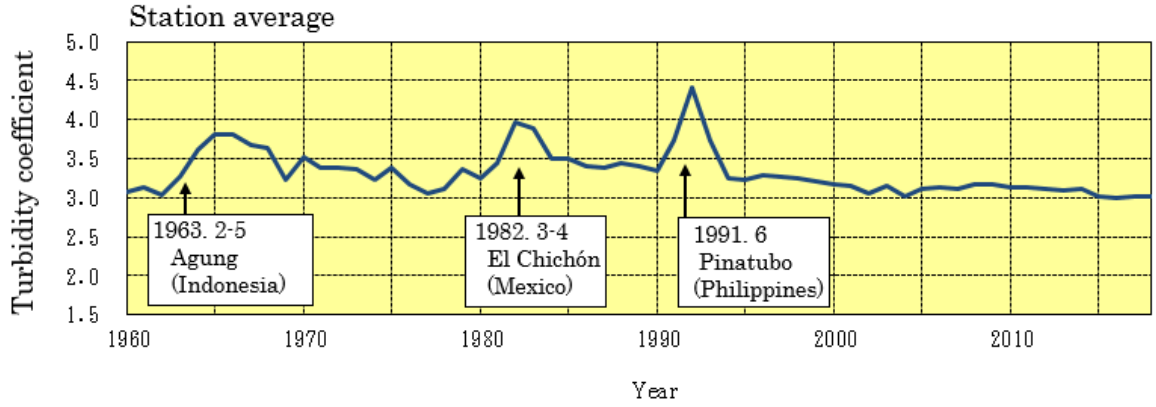

Figure 3.3-1 Time-series representation of annual mean atmospheric turbidity coefficients (1960 – 2018)
To eliminate the influence of variations in tropospheric aerosols such as water vapor, dust and air pollutants, the annual mean atmospheric turbidity coefficient is calculated using the minimum turbidity coefficient for each month.

36 See the Glossary for terms relating to aerosols.
Information on aerosols and Kosa is published on JMA's website.
https://www.jma.go.jp/en/kosa/ (Prediction and observation of Kosa)

37 The atmospheric turbidity coefficient indicates the ratio of the atmospheric optical depth affected by aerosols, water vapor and gases in the atmosphere to that uninfluenced by constituents other than air molecules such as oxygen and nitrogen in the atmosphere. Larger values indicate greater amounts of turbid matter in the air.

38 Direct solar radiation is the incident solar energy acting on the earth's surface from the sun. The atmospheric turbidity coefficient (also known as the Feussner-Dubois turbidity coefficient) can be calculated from direct solar radiation amounts.

3.3.2 Kosa (Aeolian dust)

Kosa (Aeolian dust) is a kind of aerosols that are blown up from semi-arid areas of the Asian continent and transported by westerly winds to Japan. A total of 59 JMA meteorological stations (as of 31 December 2018) perform Kosa monitoring. The phenomenon is recorded when visually observed by station staff. The number of days when any meteorological station in Japan observed Kosa was 11 in 2018 (Figure 3.3-2), and the total number of stations reporting its occurrence during the year was 104 (Figure 3.3-3).

The number of days on which Kosa is observed and the annual total number of stations reporting the phenomenon show large interannual variability. As a result, the long-term trend of occurrence remains unclear.

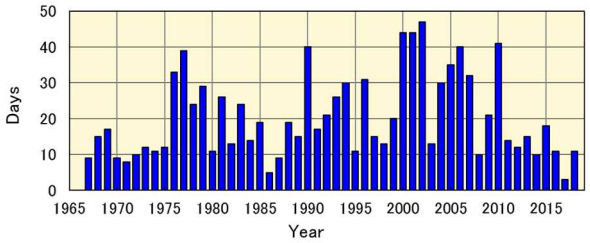

Figure 3.3-2 Number of days when any station in Japan observed Kosa (1967 – 2018) based on the 59 stations that were active for the whole period

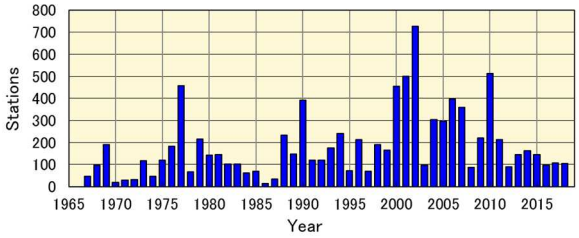

Figure 3.3-3 Annual total number of stations observing Kosa in Japan (1967 – 2018) based on the 59 stations that were active for the whole period

3.3.3 Solar radiation and downward infrared radiation

The earth's radiation budget is a source of energy for climate change, and monitoring of its variations is important. To this end, JMA conducts measurements of direct solar radiation, diffuse solar radiation and downward infrared radiation[39] at five stations in Japan (Sapporo, Tsukuba, Fukuoka, Ishigakijima and Minamitorishima) (Figure 3.3-4).

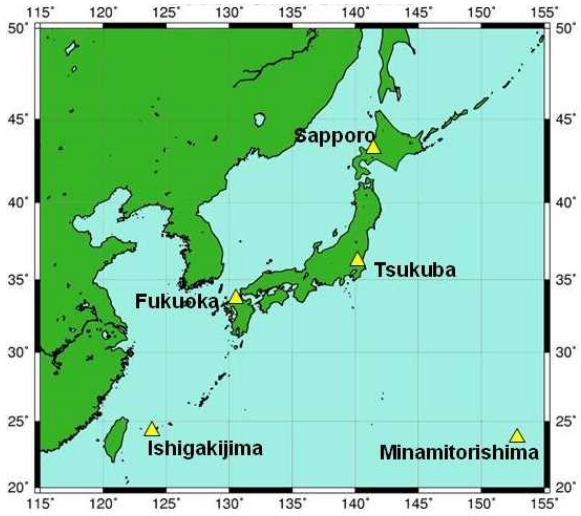

Figure 3.3-4 JMA's solar radiation and infrared radiation observation network

JMA conducts observation of direct solar, diffuse solar and downward infrared radiation at five stations (Sapporo, Tsukuba, Fukuoka, Ishigakijima and Minamitorishima).

39 Downward infrared radiation is the incident infrared radiation acting on the earth's surface from all directions in the sky. It is emitted from clouds and atmospheric constituents such as water vapor and carbon dioxide in proportion to the fourth power of their temperature, and can be used as an index of global warming.

(1) Global solar radiation

Reports indicate that global solar radiation decreased from around 1960 to the late 1980s before increasing rapidly from the late 1980s to around 2000, and no obvious changes have been observed in most regions of the world (Ohmura, 2009).

In Japan, global solar radiation declined rapidly from the late 1970s to around 1990 before increasing rapidly from around 1990 to the early 2000s. Since then, data from measurements at the five observation stations show no obvious changes. These long-term variations are consistent with those reported globally (Figure 3.3-5). Variations are considered to stem mainly from changes in anthropogenic aerosols in the atmosphere, and to be partly attributed to changes in cloud cover and cloud characteristics (Wild, 2009). Norris and Wild (2009) quantitatively estimated the cause of the rapid increase in global solar radiation observed in Japan from around 1990 to the beginning of the 2000s. According to their estimates, two thirds of the increase was due to reduced anthropogenic aerosols in the atmosphere and the other third was due to reduced cloud cover. These results imply that the presence of anthropogenic aerosols has a profound effect on solar radiation variations. Results produced by Kudo et al. (2012) indicated that the solar radiation increase was mainly caused by changes in the optical characteristics of aerosols due to changes in the aerosol composition of the atmosphere.

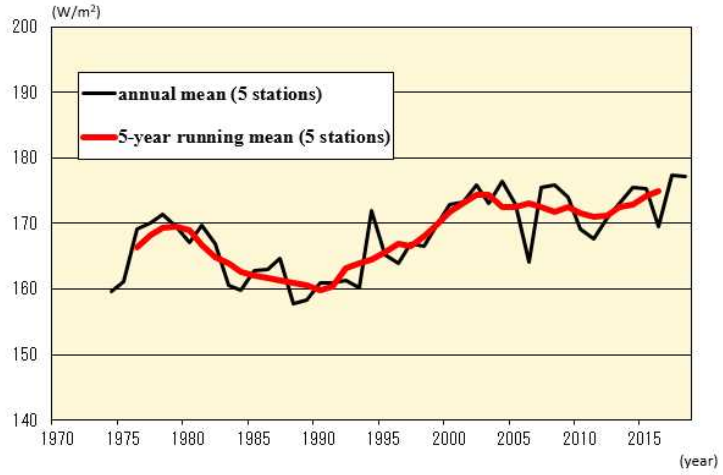

Figure 3.3-5 Time-series representations of annual and five-year-running means of global solar radiation at five stations in Japan (Sapporo, Tsukuba, Fukuoka, Ishigakijima and Minamitorishima)

(2) Downward infrared radiation

Atmospheric concentrations of carbon dioxide and other greenhouse gases, which cause global warming, show increasing yearly trends. Observation of downward infrared radiation is effective for the evaluation of global warming because signals of global warming due to increased greenhouse gases are seen more clearly from increased downward infrared radiation than from increased surface temperatures. While general circulation model experiments suggest that two decades of downward infrared radiation monitoring are necessary to detect statistically significant increases with a confidence level of 95%, analysis of in situ observation data covering about a decade has shown an overall increase (Wild and Ohmura, 2004).

In Japan, downward infrared radiation has been monitored since the early 1990s at Tsukuba. Analysis of the data obtained shows an increasing trend at a rate of about 0.3 W/m^2 per year during the period from 1993 to 2018 (Figure 3.3-6). This is consistent with the trend seen in the

results of analysis using data from 20 BSRN[40] stations worldwide (+0.3 W/m^2 per year during the period from 1992 to 2009) (WCRP, 2010).

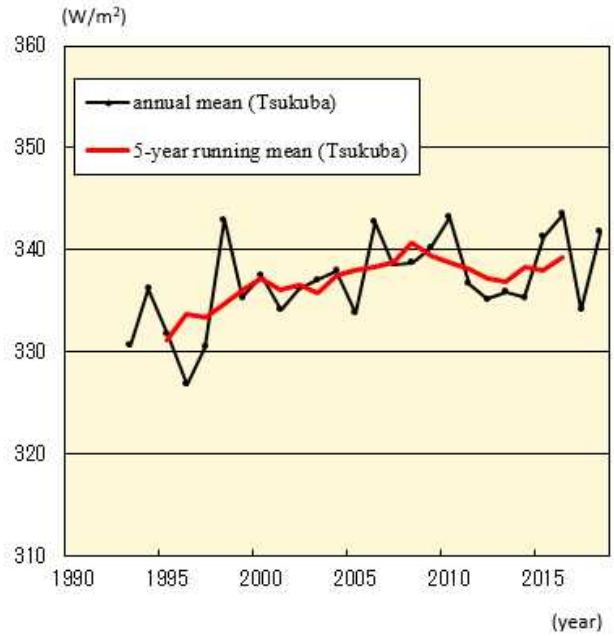

Figure 3.3-6 Time-series representations of annual and five-year-running means of downward infrared radiation at Tsukuba

40 The BSRN (Baseline Surface Radiation Network) is a global observation network for measuring high-precision surface radiation balance on an ongoing basis. JMA operates five BSRN stations in Japan (Sapporo, Tsukuba, Fukuoka, Ishigakijima and Minamitorishima) and one in Antarctica (Syowa Station).